Geophysical Research Letters

RESEARCH LETTER
10.1029/2022GL101022

Ambient Noise Tomography of the Lipari Volcanic Island (Southern Italy) From a Dense Nodal Array

Marco Calò[1], Francesca Di Luccio[2], Patricia Persaud[3,4], and Guido Ventura[2,5]

[1]Instituto de Geofísica, Universidad Nacional Autónoma de México, UNAM, Mexico City, Mexico, [2]Istituto Nazionale di Geofisica e Vulcanologia, INGV, Rome, Italy, [3]Department of Geology and Geophysics, Louisiana State University, Baton Rouge, LA, USA, [4]Department of Geosciences, University of Arizona, Tucson, AZ, USA, [5]Istituto per lo Studio degli impatti Antropici e Sostenibilitá in ambiente marino (IAS), Capo Granitola, Italy

Key Points:

- Dense nodal array probes the underground plumbing system of active volcanic islands
- Ambient noise tomography reveals the complexity of the spatio-temporal relationship between volcanic, structural, and hydrothermal features
- High and low shear wave velocities are linked to different eruptive epochs of volcanic edifices in the southern Tyrrhenian Sea

Supporting Information:

Supporting Information may be found in the online version of this article.

Correspondence to:

M. Calò,
calo@igeofisica.unam.mx;
marcoocalo@yahoo.it

Citation:

Calò, M., Di Luccio, F., Persaud, P., & Ventura, G. (2023). Ambient noise tomography of the Lipari volcanic island (Southern Italy) from a dense nodal array. *Geophysical Research Letters*, *50*, e2022GL101022. https://doi.org/10.1029/2022GL101022

Received 31 AUG 2022
Accepted 19 JAN 2023

Author Contributions:

Conceptualization: Marco Calò, Francesca Di Luccio
Data curation: Francesca Di Luccio
Formal analysis: Marco Calò
Funding acquisition: Francesca Di Luccio, Patricia Persaud
Investigation: Francesca Di Luccio, Guido Ventura
Project Administration: Francesca Di Luccio
Resources: Francesca Di Luccio, Patricia Persaud
Software: Marco Calò

Abstract We applied ambient noise tomography to continuous data recorded by a dense seismic array deployed on the volcanic island of Lipari in the southern Tyrrhenian Sea. Since most of Lipari's seismicity occurs offshore and is not evenly distributed, this technique allowed us to obtain the first high-resolution images beneath the island down to ~2.5 km depth. Results show a complex seismic structure related to the various ages and compositions of the volcanic products characteristic of the different regions of the island. High shear wave velocities are found in western Lipari, where active hydrothermal vents and N-S faults are mapped. Low wave speeds are revealed beneath southern and northeastern Lipari, where more recent volcanic activity developed along N-S dike-like structures that are aligned with rhyolitic vents. We suggest these dikes likely represent the probable pathways of future volcanic eruptions.

Plain Language Summary Recordings of Earth's background seismic noise from an array of tightly spaced instruments allow us to decipher the rocks beneath Lipari, a 37-km^2 active volcanic island in the southern Tyrrhenian Sea. In 2018, for the first time, 48 compact seismic instruments were installed on the island providing continuous recordings for about 1 month that are now used to produce the first three-dimensional model of the volcano down to ~3 km depth. The high-resolution images of Lipari show complex features that are related to the different types and ages of the volcanic rocks. Active CO_2-rich fumaroles and faults found at the Earth's surface are imaged down to depths between 0.5 and 3 km. Beneath southern and northeastern Lipari, conduits of the younger N-S aligned vents are revealed in the images and they may represent the shallower feeding system of future volcanic eruptions. With the new information from seismic imaging, we are able to better understand the three-dimensional architecture of the volcanic system and faults, which combined with surface observations will allow us to more accurately determine the potential for future activity and estimate eruptive style and minimum volumes of the eruptive products.

1. Introduction

Since the pioneering works of Shapiro et al. (2005) and Sabra et al. (2005), the application of ambient noise tomography (ANT) to reveal the seismic structure of the shallow crust at progressively higher resolution has dramatically increased. ANT has been applied from global and regional (Bensen et al., 2007; Haned et al., 2016; Spica et al., 2016; Yang et al., 2008; and references therein) to local scales (Brenguier et al., 2007; Calò et al., 2013; Mordret et al., 2019; and references therein) demonstrating its great flexibility to image Earth structure. ANT is now a well-established technique and involves four main steps: (a) reconstruction of the empirical Green's functions (GFs) from the cross-correlation of seismic records at station pairs, (b) picking of the dispersion curves of the reconstructed surface waves, (c) computation of the 2D tomograms and, (d) inversion of the dispersion curves to retrieve a pseudo-3D shear wave velocity (V_S) model. Thus, the pre-processing steps can be performed either in the time or frequency domain (Bensen et al., 2007) or using the phase representation (Schimmel et al., 2011; Ventosa et al., 2017). Additionally, some authors simultaneously combine the computation of the 2D tomograms and depth inversion with the direct inversion of the dispersion curves into a final 3D model (e.g., Cruz-Hernández et al., 2022; Fang et al., 2015). ANT has then evolved to become a valid complement to more traditional tomographic techniques.

Three-dimensional images of the seismic structure from ANT depend on the number, distribution, operational time, sampling rate, and frequency range of the sensors used. The interstation distance along with the

Supervision: Marco Calò, Francesca Di Luccio, Guido Ventura
Validation: Marco Calò
Visualization: Marco Calò, Guido Ventura
Writing – original draft: Marco Calò, Francesca Di Luccio, Guido Ventura
Writing – review & editing: Marco Calò, Francesca Di Luccio, Patricia Persaud, Guido Ventura

characteristics of the seismic instrumentation provide the frequency range of the dispersion curves and therefore account for the resolution and sensitivity of the resulting velocity model.

In volcanic regions, ANT has been applied to a wide range of settings, from basaltic hotspots and rift volcanoes (Brenguier et al., 2007; Jeddi et al., 2017) to rhyolitic, andesitic, and more complex subduction-related strato-volcanoes (Cabrera-Perez et al., 2022; Calò et al., 2021; Spica et al., 2017; and references therein) and calderas (De Siena et al., 2018; Granados-Chavarría et al., 2022; Stankiewicz et al., 2010). ANT is particularly useful in volcanic areas where standard tomographic techniques are not appropriate due to sparse seismicity and/or to very localized event clusters.

The spatial extent of the seismic survey, the total number of stations, and the station-spacing depend on the size of the volcano and the accessibility of areas with steep and rugged topography. Because of the geographical constraints, ANT with more than 20–25 stations and interstation distance of a few kilometers remains a growing direction in volcano imaging (Cabrera-Pérez et al., 2022; Matos et al., 2015; Wang et al., 2017) with volcanic islands presenting more challenges than continental settings. Since the surrounding sea further restricts the extent of passive seismic experiments at volcanic islands, this limits the spatial resolution of the tomographic images. Therefore, only few volcanic islands have been investigated with sufficient ray path coverage to ensure reliable and detailed reconstruction of the underlying structure.

The volcanic island of Lipari located in the southern Tyrrhenian Sea, Italy last erupted in 1220 CE (Forni et al., 2013). Lipari's surface above sea level is about 37 km^2 with the longest dimensions of 9 and 7 km in the N-S and E-W directions, respectively (Figure 1). Although the small extent of the island makes it difficult to plan a seismic experiment to investigate the velocity structure, using ANT, a dense array allows for a detailed reconstruction of the volcano features at least in the upper 2–3 km depth.

In this study, we produce the first 3D velocity model of Lipari Island using recordings from a dense array of 48 seismic nodes installed on the subaerial part of the volcano (Di Luccio et al., 2019). The high-quality data allowed us to extract dispersion curves from the empirical GF in the 0.25–5 Hz frequency range. For the first time, the detailed velocity structure from the surface to about 2.5 km depth is obtained, imaging the shape and the relationship among the different volcanic and tectonic structures of the island.

2. Geological and Geophysical Setting

The Aeolian arc consists of seven volcanic islands and seamounts located in the southern Tyrrhenian back-arc basin. The southern Tyrrhenian back-arc developed in the last 2 Ma and is associated with the subduction and roll-back of the oceanic Ionian lithosphere below the Calabrian Arc, in the general framework of the Eurasia-Africa plate convergence (Figure 1). At the regional scale, tomographic images of the Tyrrhenian subduction zone show a nearly continuous, subvertical slab dipping 70°–80° north-westward, which is also supported by the deep seismicity that reaches 500 km depth (Calò et al., 2012; Chiarabba et al., 2008). Hypocenters of the deeper earthquakes follow the north-westward dipping slab and are laterally distributed from northern Calabria to eastern Sicily. The major fault system in the Tyrrhenian region is the NNW-SSE strike-slip Tindari-Letojanni fault (TLf) (De Astis et al., 2003) that represents a deep crustal discontinuity interpreted as a Subduction-Transform Edge Propagator (STEP) fault that laterally bounds the western edge of the rolling-back slab (Govers & Wortel, 2005).

Salina, Lipari, and Vulcano, the islands of the central Aeolian Arc (insets of Figure 1), are aligned with the TLf and were emplaced on 20-km-thick continental crust (Ventura et al., 1999). At Lipari island, volcanic rocks and deeper intrusions fill a ~3-km-deep structural depression (Barberi et al., 1994). According to Forni et al. (2013), the volcanic activity of Lipari developed between 267 ka and historical times (1220 CE). The early activity mainly consists of basaltic to andesitic lava flows and scoria deposits, while the final stages include the extrusion of rhyolitic domes, explosive eruptions including sub-Plinian events, and the emplacement of pumice cones and obsidian lava flows. Lipari's volcanism can be divided into nine eruptive epochs (EEs) separated by periods of quiescence. EEs 1– 3 (271–188 ka) include the activity of the N-S aligned Chiesa Vecchia, Mazzacaruso, Timpone Ospedale, Timpone Carrubo, and Mt. Chirica volcanoes, which are in the western sector of the island (Figure 1). EEs 4– 6 (119–81 ka) are characterized by the formation of the Mt. S. Angelo volcano in the central part of the island, a second phase of activity of Mt. Chirica volcano, and the growth of Mt. Rosa volcanoes located in eastern Lipari (Figure 1).

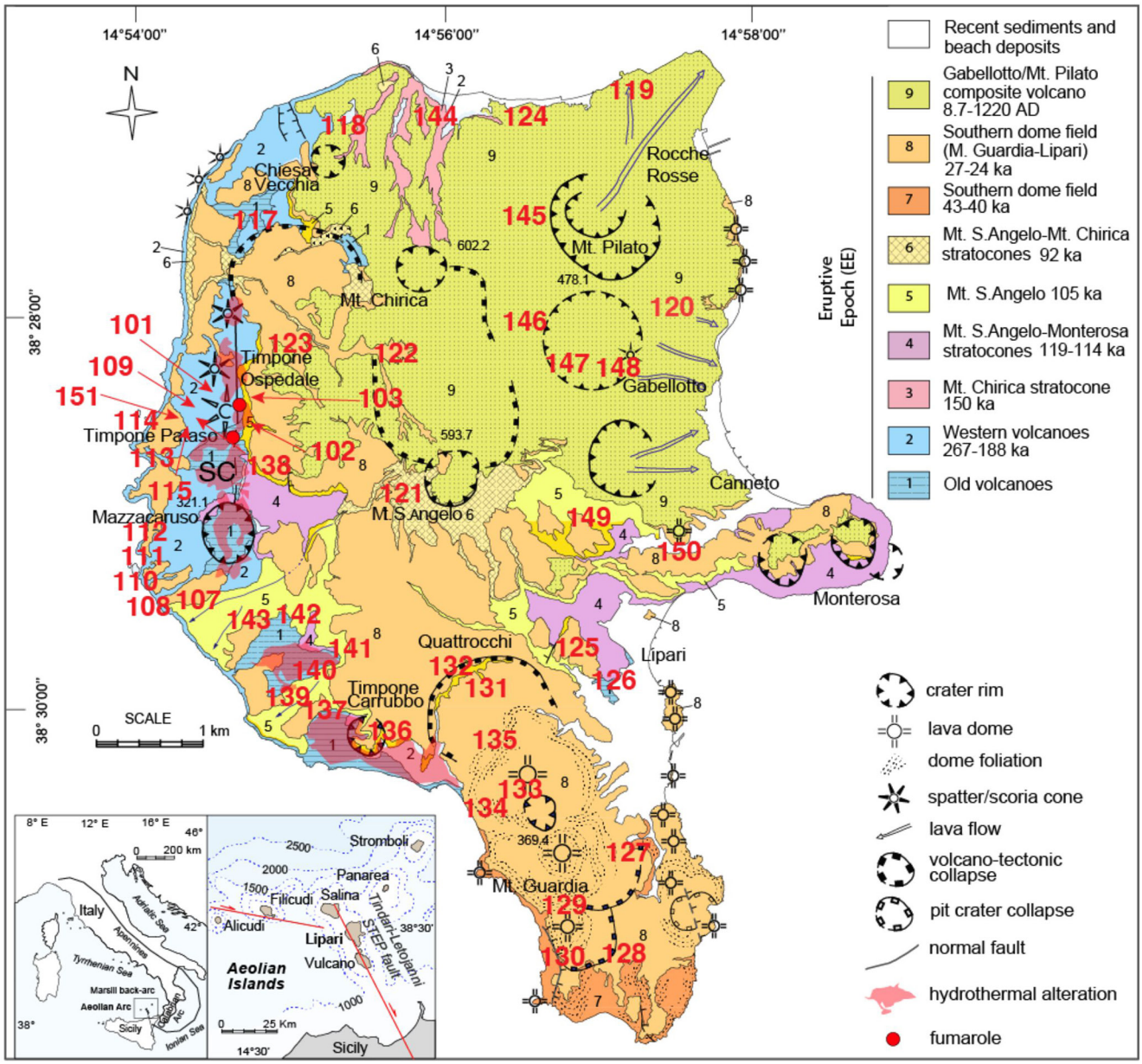

Figure 1. Geological map of Lipari Island (modified from Forni et al., 2013, 2015) in the southern Tyrrhenian Sea. The location of the Aeolian Arc is shown in the insets at the bottom left and the main tectonic structures are also shown in red. In the large map, red numbers indicate the locations of the seismic nodes, while SC shows the hydrothermal area of San Calogero that is located just south of the fumaroles (red filled circles in western Lipari).

Explosive eruptions and the extrusion of N-S to NNW-SSE aligned lava domes characterize EEs 7 and 8 between 67–70 and 19–24 ka (Figure 1). This volcanism occurred mainly in the southern part of the island, while the EE 9 activity, which developed between 8.7 and 8.4 ka and 1220 CE, includes the emplacement of obsidian lava and pumice cones (Vallone Gabellotto and Mt. Pilato in Figure 1). The pyroclastic products of EEs 7– 9 cover most of the central and northern sectors of the island (Figure 1). The post-42 ka vents align along N-S direction. An active hydrothermal system with fumaroles (Timpone Ospedale) and an up to 500 m wide kaolin and gypsum hydrothermal alteration zone characterizes the westernmost region of Lipari (Cucci et al., 2017). This area extends from the oldest vents (Timpone Ospedale) southward to Timpone Carrubbo (Figure 1) across a distance of about 3 km and is structurally controlled by N-S striking faults and associated gypsum-filled veins. Fumaroles are located in northern Lipari close to Timpone Ospedale (Figure 1) and the emitted gases are dominated by carbon dioxide of magmatic origin with equilibrium temperatures of 170–180°C, while the SO_4^{2-} content is about 780 ppm (Cioni

et al., 1988). Cap rocks of the ~1 to 4.6-km-deep geothermal reservoir are relatively shallow and include the lacustrine and clay-rich deposits that outcrop on the island (Bruno et al., 2000). Faults and fractures in western Lipari create pathways for ascending hydrothermal fluids (Figure 1). The 550–580°C Curie isotherm of the island is very shallow and has been estimated at about 1 km depth (De Ritis et al., 2013).

Structural and seismic data indicate that Lipari and the neighboring Vulcano are mainly controlled by the TLf system (inset of Figure 1) although secondary NE-SW and N-S striking faults are also present (Barreca et al., 2014; De Astis et al., 2003; Mazzuoli et al., 1995; Ruch et al., 2016; Ventura et al., 1999). The seismicity of Lipari is concentrated along the TLf and the largest earthquake in 1978 (M 5.6) had a focal mechanism consistent with dextral strike-slip movement of the TLf-STEP faults (Barreca et al., 2014; Neri et al., 1996). This kinematics fits with the N-S compression and E-W extension obtained from the stress inversion of regional earthquake focal mechanisms (Cintorrino et al., 2019).

Although geophysical studies have imaged the structure of the Aeolian islands at the regional scale, the seismic structure of Lipari remained poorly understood due to the lack of a dense seismic network on the island. However, in 2018, a seismic array of 48 cable-free nodes was installed on Lipari to monitor the seismicity (Di Luccio et al., 2019). Swarm-like and hybrid events confirmed ongoing activity deep within the hydrothermal systems (Di Luccio et al., 2021).

3. Data and Methods

The ANT of Lipari is carried out using data from the 2018 dense array of FairfieldNodal ZLand three-component nodes (Di Luccio et al., 2019, 2021). The nodes have a 5 Hz low-corner frequency and 46 of the 48 nodes acquired continuous data at 250 samples per second (sps) for about 30 days. The Lipari array covered the whole island with interstation distances from 0.1 to 8.5 km (Figure 1, Figure S1 in Supporting Information S1). To retrieve the dispersion curves of the Rayleigh waves, we apply the cross-correlation method to the vertical component of the continuous records. We do not remove the instrument response because all sensors are the same (Cole, 2019; Liu et al., 2018, details on the data processing are reported in the Supporting Information). Data are resampled at 20 sps and filtered between 0.2 and 10 Hz assuming the lowest group velocity is 0.7 km/s and the largest interstation distance is 8.5 km. Data processing follows the scheme proposed by Bensen et al. (2007) and modified by Granados-Chavarría et al. (2022). Daily records are cut into 30-min time windows and one-bit normalization and spectral whitening are applied to each time window. The final cross-correlations are obtained by first stacking the 48 cross-correlations of each day and then stacking the retrieved signals over all available days (Figure S1 in Supporting Information S1).

The group velocity dispersion curves are manually picked using the Noisy Dispersion Curve Picking program (NDCP; Granados et al., 2019). NDCP allows for the analysis of the correlation functions in both the frequency and time domains, thus providing better control of the several parameters that have to be set to identify group velocity dispersion at a very local scale (Figure S2 in Supporting Information S1). We are able to pick 776 of the 1,035 potential dispersion curves associated with all combinations of station pairs. Because of the small interstation distance, we estimate the dispersion patterns in the 0.25–3 s period range (Figure S3 in Supporting Information S1). Dispersion maps at different periods are obtained using a modified version of the 2D ray-based tomography approach proposed by Barmin et al. (2001) that accounts for the station elevation during the calculation of the travel times along the ray paths (Calò et al., 2021). The cell size of the 2D maps is fixed at 550 m × 550 m for the analyzed periods, while damping and smoothing of the inversion (Hansen, 1992) have been optimized for each tomogram. Resolution tests show the stability and resolution of the inversion procedure (Figure S4 in Supporting Information S1; Sieminsky et al., 2004, more details in the Supporting Information).

Finally, we reconstructed the dispersion curve for each cell using the 2D maps (Figure S5 in Supporting Information S1), and computed the 1D V_S model at each location in the grid. We adopted the method described by Haney and Tsai (2017) that uses a perturbational and non-perturbational inversion scheme of the Rayleigh wave velocities to estimate the 1D V_S structure (Figure S6 in Supporting Information S1). The procedure consists of a first inversion that uses the non-perturbational method based on the Dix approximation (Dix, 1955) to set the velocity space in which data are inverted by applying the perturbational approach. Therefore, no a-priori discontinuities are provided but only a suitable space where the perturbation of the wavenumber and material properties is done using the finite element approach by fixing the frequency (Haney & Tsai, 2017). Synthetic tests corroborate

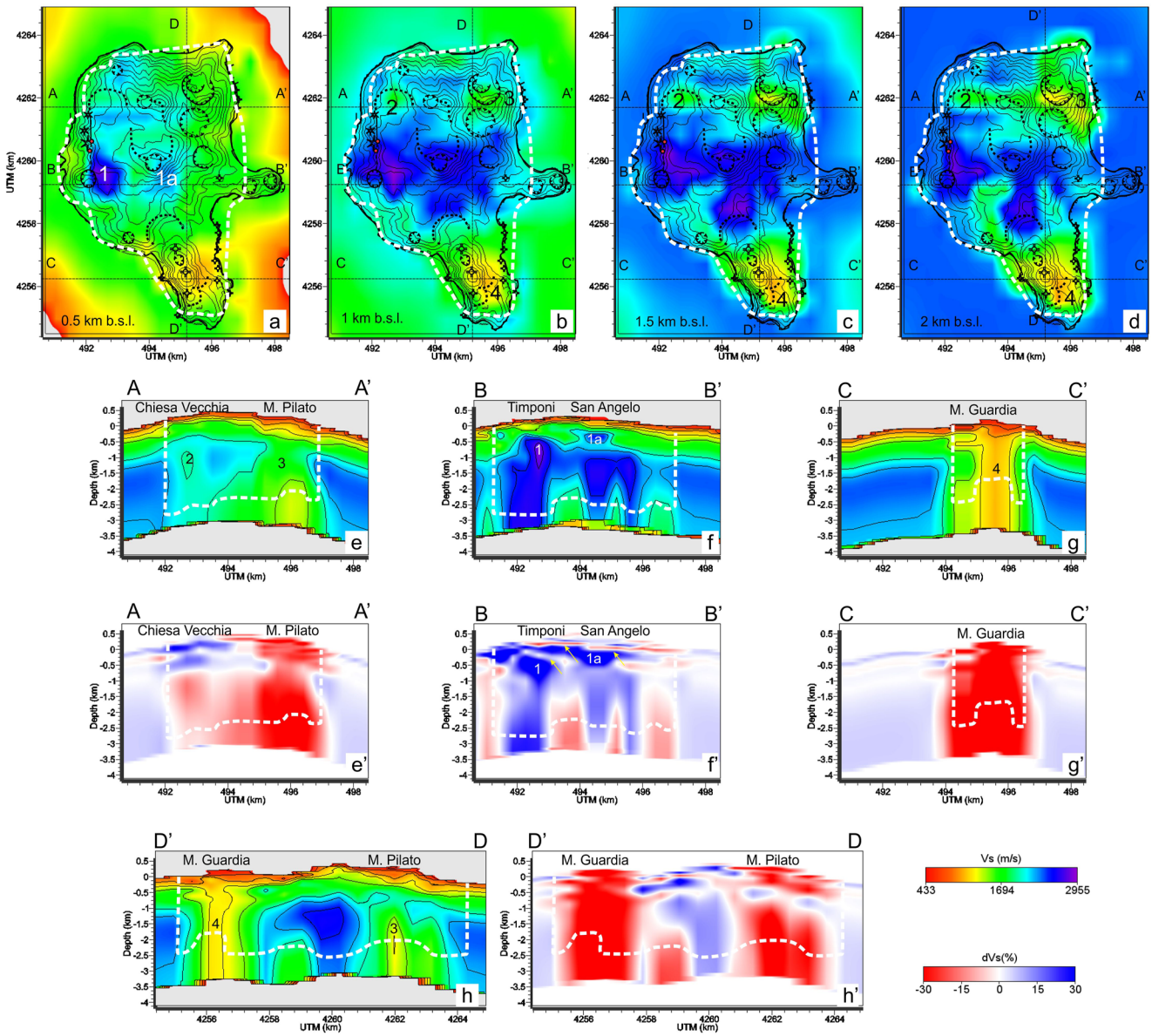

Figure 2. (a–d) Shear wave velocity maps at different depths below sea level as indicated in the bottom left of each panel. Locations of the W-E (AA′, BB′, and CC′) and N-S (DD′) profiles are plotted as black dashed lines. Shear wave velocities (e–h) and anomalies (e′–h′) in W-E (AA′, BB′, and CC′) and N-S (DD′) cross-sections, respectively. Numbers in the plots indicate the velocity anomalies (low and high) calculated with respect to the 1D average model (Figure S6a in Supporting Information S1), whereas white dashed lines outline the well-resolved region according to the synthetic tests (Figure S4 in Supporting Information S1) and sensitivity kernels of the considered periods at each cell of the mesh used (Figure S6 in Supporting Information S1).

the possibility to reproduce thin low/high velocity layers at shallow depths observed during the inversion of the observational data (Figures S7 and S8 in Supporting Information S1).

All 1D V_S profiles are then merged into a 3D model taking into account the topography of the island. Sensitivity kernels of the 1D models (Figure S6 in Supporting Information S1) suggest that the period range used for the depth inversion (0.25–3 s) is sensitive to the structure down to about 2.5 km depth.

4. Results

The 3D velocity model of Lipari is displayed in four depth slices (Figures 2a–2d) of 0.5, 1, 1.5, and 2 km below sea level (bsl), respectively, and in four vertical profiles (Figures 2e–2h) that are representative of the main

features of the island. At 0.5-km depth, a high V_S body (label 1 in Figure 2) is located just below the San Calogero hydrothermal area, near the Mazzacaruso crater and the kaolin outcrops. This anomaly extends in the E-W direction down to 2 km depth separating the island into three main regions. In the northernmost region, low velocities are mainly concentrated south of Chiesa Vecchia and beneath Mt. Pilato (labels 2 and 3 in Figure 2), whereas in the southernmost part of the island, low V_S regions are located below Mt. Guardia (label 4 in Figure 2b).

Vertical cross-section AA′ (Figure 2e) extending from Mt. Chirica to Mt. Pilato shows low V_S beneath these craters in the well-resolved model (labels 2 and 3 of Figure 2). Noteworthy is that the region beneath Mt. Pilato has lower V_S values (∼1,500 m/s) than the one beneath Mt. Chirica (∼2,000 m/s). Furthermore, a representation of the model in terms of anomalies with respect to the 1D average model (Figure S6a in Supporting Information S1) shows that the velocity anomaly beneath Mt. Chirica ends at 0.7 km bsl whereas the one beneath Mt. Pilato extends to shallower depths. Cross-section BB′ crosses the high velocities observed in the central part of the island from west to east. Here, high V_S values are restricted to below 0.6 km bsl, while beneath Mazzacaruso and near Mt. S. Angelo the high V_S regions reach shallower depths, 0.3 and 0.2 km bsl, respectively (labels 1 and 1a in Figure 2). At the top of these high V_S bodies, two thin layers of relatively low-velocity anomalies (yellow arrows in BB′ in Figure 2f) are clearly imaged. At greater depth, some V_S lows are observed, although their shape and intensity may be uncertain because of the lower resolution of the model at those depths.

Cross-section CC′ shows a single subvertical low V_S feature just beneath Mt. Guardia at all depths of the model (label 4 in Figure 2).

The N-S profile, DD′ highlights the two main low-velocity patches located beneath Mt. Guardia (to the south) and Mt. Pilato (to the north), respectively (labels 3 and 4 in Figure 2). As already observed in the depth slices, a high V_S volume separates the northernmost and the southernmost sectors of the island.

5. Discussion and Conclusions

The pattern of the V_S anomalies at Lipari clearly resolves a large high velocity (1.8 km/s < V_S < 2.9 km/s) volume beneath the central part of the island at 0.5–2 km depth (Figure 2 1–2 km depth and Figure 2f). To the west, the location of this volume coincides with the older volcanoes of EEs 1 and 2 (Timpone Ospedale, Timpone Pataso, and Mazzacaruso; Figure 1), and in central and eastern Lipari with M. S. Angelo and Monterosa of EEs 3 and 4, respectively. Since the compositions of the erupted products of these volcanoes range from basalts to andesites (Forni et al., 2013), the high V_S anomalies are associated with the intrusive bodies of shallow and fully crystallized reservoirs of the older Lipari volcanoes. From the petrologic and mineral physics database (Sowers & Boyd, 2019), the different composition of igneous rocks at standard pressure and temperature conditions and assuming no anelasticity and zero porosity indicates higher V_S values for basalts than for rhyolites. Empirical relationships of Brocher (2005) for V_S as a function of V_P confirm this trend in the near surface (depth < 5 km). Lesage et al. (2018), comparing the seismic velocity models of the shallow structure of volcanoes, laboratory velocity measurements on rock samples, and sonic logs from deep boreholes, shows that the strong variability of seismic velocities depends on the diverse complexity of volcanic materials. In general, the proposed model indicates that very low velocities at the surface and a strong velocity increase in the first few hundred meters below the surface describes well the velocity variations in the 500-m-thick shallow layer for andesitic and basaltic volcanoes (Lesage et al., 2018). At shallow depths (<1 km), the high V_S patches concentrated below Mazzacaruso and Mt. S. Angelo and may represent the uppermost apophysis of the above-mentioned reservoirs, that is, the volcanic conduits, which are dike-like shaped in the case of Mazzacaruso (Forni et al., 2013). The pronounced high V_S anomalies 1 and 1a near Mazzacaruso and Mt. S. Angelo (Figure 2f) may be due to the close spatial association of the basaltic to andesitic rocks of EEs 1–3 and the vapor-saturated rocks corresponding to the active hydrothermal system observed at the surface. The presence of thermal waters and fumaroles (Cioni et al., 1988), clay-rich deposits (kaolin) due to hydrothermal alteration (Cucci et al., 2017) as well as cap rocks consisting of lacustrine and welded pyroclastic successions (Bruno et al., 2000), support the hypothesis that these high V_S anomalies (label 1 in Figure 2) are associated with the hydrothermal CO_2-rich fluids stored in basaltic rocks at 1 km depth in the Mazzacaruso-Timponi area (Cucci et al., 2017). The sub-horizontal and thin low V_S layers at sea level just above anomalies 1 and 1a (yellow arrows in Figure 2f) can be interpreted as the clay caps that seal the hydrothermal system reducing activity at the surface, in agreement with field and geophysical data (Bruno et al., 2000; Cucci et al., 2017). In fact, the shape of anomaly 1 (Figure 2) seems to fit with the N-S striking fault

in the western sector of the island (Figure 1) and, along with its alignment with hydrothermal activity at the surface, this fault appears to control fluid ascent in this area (Cucci et al., 2017).

The subvertical low-velocity zone 2 (Figure 2; $V_S \sim 1.6$ km/s), located just beneath the Mt. Chirica volcano (Figure 2), may also be interpreted as a volcanic conduit formed by highly fractured and/or hydrothermally altered rocks with respect to those composing the Timponi and Mt. S. Angelo conduits. This interpretation accounts for the lower V_S values of this conduit-like structure relative to zones 1 and 1a, and is supported by the laboratory results of low V_S measurements in fractured rocks relative to intact rocks (Saroglou & Kallimogiannis, 2017).

Low V_S (<1.4 km/s) regions 3 and 4 (Figure 2) at depths between 1 and 2 km, underlie the younger volcanoes of Lipari, which are the Mt. Pilato-Gabellotto pumice cones and obsidian lava flows (EE 9) and the southern Lipari domes (EEs 7 and 8). These more recent volcanoes are characterized by SiO_2-rich products (rhyolite). In cross-sections, CC′ and DD′ of Figures 2g and 2h, the negative V_S anomalies depict conduit-like shapes and may be interpreted as shallow conduits of the rhyolitic centers in the island.

The low velocity of such conduits may be due to the occurrence of highly fractured and/or altered rocks as well as the existence of low-density rhyolitic products. This latter interpretation is supported by the inverse relationship between the SiO_2 content of volcanic rocks and the V_S values detected in many volcanoes worldwide (Lesage et al., 2018). The shallower and thin low-velocity layer mantling Lipari may correspond to rocks of past pyroclastic sequences covering a large part of the island, and, in particular, those related to the Mt. Guardia, Mt. S. Angelo, and Mt. Pilato explosive activity.

V_S anomalies beneath Lipari (Figure 2) show that the conduits of the younger volcanoes consist of N-S dike-like (southern Lipari domes) or aligned subcircular (Mt. Pilato-Gabellotto) conduits. This arrangement supports the structural model of Ventura et al. (1999) and Ruch et al. (2016), which suggest that during the recent phases of volcanism on Lipari and the neighboring Vulcano island, magmas ascended to the surface along a major N-S structural discontinuity associated with the E-W extension and N-S compression of the central-southern sector of the Aeolian arc.

The thin, sill-like low V_S anomalies located above the N-S elongated dikes at depths less than 0.5–1 km structurally coincide with the interface between lava flows and the overlying sediments and pyroclastic rocks (Forni et al., 2013). This lithological discontinuity may favor the lateral instead of vertical migration of ascending magma because lavas can act as rigidity barriers (Townsend et al., 2017). This mechanism has been invoked to explain the lateral migration of vents observed at the Etna volcano, Italy (Nicolosi et al., 2014). We conclude that the V_S anomalies at Lipari reflect the change in the geometry of the shallower plumbing system.

In the 3D views of Figure 3, we show two nearly sill-like, low V_S volumes that flatten out at about 500 m depth and are connected to deeper (>1 km depth) N-S aligned dike-like structures. Such structures correspond with the N-S trending gravity minima of Lipari (Barberi et al., 1994). Two low-velocity patches underlie the Mt. Guardia domes to the south and Mt. Pilato-Gabellotto vents to the north. The high V_S volumes in western Lipari reveal an N-S trending dike-like structure below the Timponi and Mazzacaruso area, as reported by Forni et al. (2013). This volume is associated with a N-S gravity maximum (Barberi et al., 1994) in the western sector of the island where a N-S striking, ∼2 km long, fault zone is mapped. Although *V*s alone cannot fully constrain petrophysical properties, we interpret these N-S negative and positive velocity anomalies as dike structures characterized by different chemical compositions. The rhyolites of Mt. Pilato-Gabellotto and southern Lipari account for the negative *V*s anomalies while basalts beneath Timponi and Mazzacaruso to the west account for the positive *V*s anomalies. This difference may also explain the different gravity anomalies in the two locations.

In summary, the 3D imaging of Lipari depicts a complex shallow V_S structure revealing the close spatial and temporal relationship among different volcanic, structural and hydrothermal features. This complexity is due to the coexistence of (a) partly superimposed volcanoes with different structures, for example, a central polygenic edifice (Mt. S. Angelo), small-scale scoria and pumice cones (Timponi, Mt. Pilato), and domes (Mt. Guardia), (b) erupted products with extremely variable compositions, for example, early basalts and basaltic andesites and later andesites, dacites and rhyolites, (c) areas of intense hydrothermal activity, and (d) zones affected (or not) by faults.

Our data indicate that the more recent volcanic activity developed in N-S dike-like structures along which the more recent (<24 ka) rhyolitic vents align, as also observed in previous geological data (Forni et al., 2013;

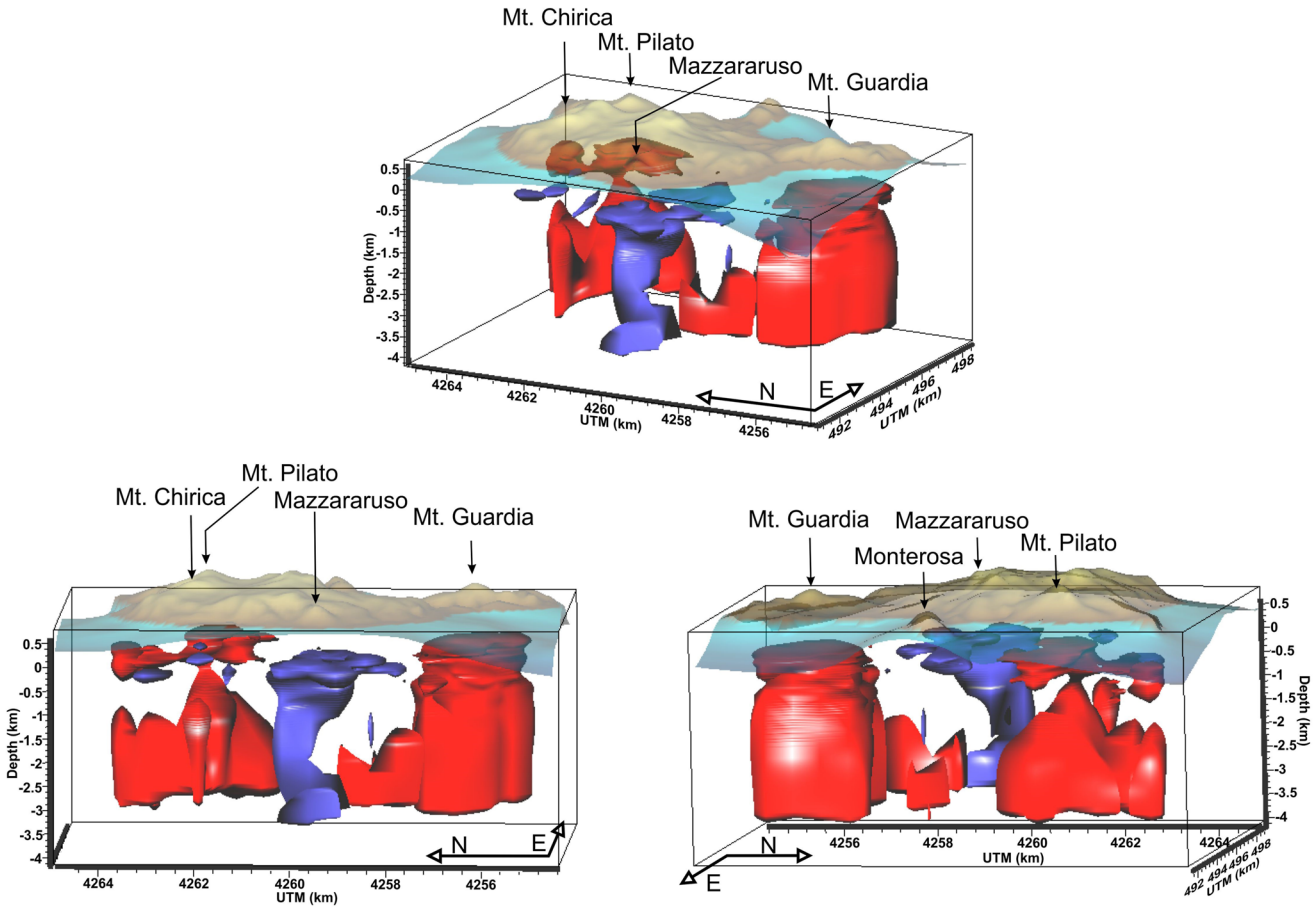

Figure 3. Three-dimensional views of the low (red) and high (blue) shear wave velocity volumes beneath Lipari island. Isovelocity contours are ±17% with respect to the 1D average model (Figure S6a in Supporting Information S1). The topography of the island is also shown at the top of each plot.

Ventura et al., 1999). Therefore, we propose that such dikes may represent the preferred pathways of future volcanic eruptions. This conclusion suggests the importance of starting the continuous monitoring of Lipari to detect the possible temporal variations of geophysical and geochemical observables. The results of the 2018 seismic experiment presented in this study demonstrate that dense nodal arrays can provide high-quality data sets, useful for studying the velocity structure of volcanically active and densely populated islands. Such rapid low-cost deployments further allow for the time-lapse monitoring of volcanic and hydrothermal systems for near real-time hazard assessment.

Data Availability Statement

The empirical Green's functions described in the study are freely available at the repository named "cross-correlations of seismic data nodes Lipari 2018" on the platform https://www.zenodo.org (https://doi.org/10.5281/zenodo.7036194). Empirical Green's functions and dispersion maps were calculated using matlab functions (MATLAB 2017a, The MathWorks, Inc., Natick, MA, United States). Dispersion curves were measured using the freely available NDCP suite (Granados et al., 2019; https://github.com/IvanGCh/NDCP). Depth inversions were calculated using the freely available Raylee code (Haney & Tsai, 2017; https://github.com/matt-haney/raylee_codes). Some figures were generated using Voxler® from Golden Software, LLC (www.goldensoftware.com).

Acknowledgments
The authors thank two anonymous referees and Editor Dayoun Sun for their useful comments and suggestions. This work was funded by the Istituto Nazionale di Geofisica e Vulcanologia, sezione di Roma 1, the Department of Geology and Geophysics of Louisiana State University, and partially supported by the "Pianeta Dinamico" call, 2023–2025 CAVEAT Project. M.C. was supported by UNAM PASPA–DGAPA. The 2018 Lipari array deployment was supported and funded by the Istituto Nazionale di Geofisica e Vulcanologia, sezione di Roma 1 and partly supported by the Department of Geology and Geophysics of Louisiana State University. The authors thank L. Cucci and A. Esposito of INGV for taking part in the 2018 Lipari array experiment.

References

Barberi, F., Gandino, A., Gioncada, A., La Torre, P., Sbrana, A. A., & Zenucchini, C. (1994). The deep structure of the Eolian arc (Filicudi-Panarea-Vulcano sector) in light of gravity, magnetic and volcanological data. *Journal of Volcanology and Geothermal Research*, *61*(3–4), 189–206. https://doi.org/10.1016/0377-0273(94)90003-5

Barmin, M. P., Ritzwoller, M. H., & Levshin, A. L. (2001). A fast and reliable method for surface wave tomography. *Pure and Applied Geophysics*, *158*(8), 1351–1375. https://doi.org/10.1007/PL00001225

Barreca, G., Bruno, V., Cultrera, F., Mattia, M., Monaco, C., & Scarfì, L. (2014). New insights in the geodynamics of the Lipari–Vulcano area (Aeolian Archipelago, southern Italy) from geological, geodetic and seismological data. *Journal of Geodynamics*, *82*, 150–167. https://doi.org/10.1016/j.jog.2014.07.003

Bensen, G. D., Ritzwoller, M. H., Barmin, M. P., Levshin, A. L., Lin, F., Moschetti, M. P., & Yang, Y. (2007). Processing seismic ambient noise data to obtain reliable broadband surface wave dispersion measurements. *Geophysical Journal International*, *169*(3), 1239–1260. https://doi.org/10.1111/j.1365-246x.2007.03374.x

Brenguier, F., Shapiro, N. M., Campillo, M., Nercessian, A., & Ferrazzini, V. (2007). 3-D surface wave tomography of the Piton de la Fournaise volcano using seismic noise correlations. *Geophysical Research Letters*, *34*(2), L02305. https://doi.org/10.1029/2006GL028586

Brocher, T. M. (2005). Empirical relations between elastic wavespeeds and density in the Earth's crust. *Bulletin of the Seismological Society of America*, *95*(6), 2081–2092. https://doi.org/10.1785/0120050077

Bruno, P. P. G., Paoletti, V., Grimaldi, M., & Rapolla, A. (2000). Geophysical exploration for geothermal low enthalpy resources in Lipari island, Italy. *Journal of Volcanology and Geothermal Research*, *98*(1–4), 173–188. https://doi.org/10.1016/s0377-0273(99)00183-3

Cabrera-Pérez, I., Centeno, R., Soubestre, J., D'Auria, L., Rivera, M., & Machacca, R. (2022). Ambient noise tomography of Misti volcano, Peru. *Journal of Volcanology and Geothermal Research*, *426*, 107538. https://doi.org/10.1016/j.jvolgeores.2022.107538

Calò, M., Kinnaert, X., & Dorbath, C. (2013). Procedure to construct three-dimensional models of geothermal areas using seismic noise cross-correlations: Application to the Soultz-sous-Forêts enhanced geothermal site. *Geophysical Journal International*, *194*(3), 1893–1899. https://doi.org/10.1093/gji/ggt205

Calò, M., Mazariegos, E. A. L., Tramelli, A., & Orazi, M. (2021). Hydrothermal systems characterization of the Stromboli volcano using spatial and temporal changes of the seismic velocities. *Journal of Volcanology and Geothermal Research*, *411*, 107177. https://doi.org/10.1016/j.jvolgeores.2021.107177

Calò, M., Parisi, L., Luzio, D., Rotolo, S. G., & D'Anna, G. (2012). Seismic velocity structures of Southern Italy from tomographic imaging of the Ionian slab and petrological inferences. *Geophysical Journal International*, *191*(2), 751–764. https://doi.org/10.1111/j.1365-246X.2012.05647.x

Chiarabba, C., De Gori, P., & Speranza, F. (2008). The southern Tyrrhenian subduction zone: Deep geometry, magmatism and Plio-Pleistocene evolution. *Earth and Planetary Science Letters*, *268*(3–4), 408–423. https://doi.org/10.1016/j.epsl.2008.01.036

Cintorrino, A. A., Palano, M., & Viccaro, M. (2019). Magmatic and tectonic sources at Vulcano (Aeolian Islands, Southern Italy): A geodetic model based on two decades of GPS observations. *Journal of Volcanology and Geothermal Research*, *388*, 106689. https://doi.org/10.1016/j.jvolgeores.2019.106689

Cioni, R., Corazza, E., Magro, G., Guidi, M., & Marini, L. (1988). Reactive and inert gases in low temperature fumaroles (Aeolian islands, Italy). *Rendiconti Societa Italiana di Mineralogia e Petrologia*, *43*, 1003–1011.

Cole, R. (2019). Using nodal seismic sensors to estimate seismic moment tensors. Technical Report (A). Retrieved from http://hdl.handle.net/11122/10676

Cruz-Hernández, F., Gallardo, L. A., Calò, M., Castro, R. R., & Romo-Jones, J. M. (2022). Laterally constrained surface wave inversion. *Geophysical Journal International*, *230*(2), 1121–1131. https://doi.org/10.1093/gji/ggac108

Cucci, L., Di Luccio, F., Esposito, A., & Ventura, G. (2017). Vein networks in hydrothermal systems provide constraints for the monitoring of active volcanoes. *Scientific Reports*, *7*(1), 146. https://doi.org/10.1038/s41598-017-00230-8

De Astis, G., Ventura, G., & Vilardo, G. (2003). Geodynamic significance of the Aeolian volcanism (Southern Tyrrhenian Sea, Italy) in light of structural, seismological, and geochemical data. *Tectonics*, *22*(4). 1040. https://doi.org/10.1029/2003TC001506

De Ritis, R., Ravat, D., Ventura, G., & Chiappini, M. (2013). Curie isotherm depth from aeromagnetic data constraining shallow heat source depths in the central Aeolian Ridge (Southern Tyrrhenian Sea, Italy). *Bulletin of Volcanology*, *75*(4), 710. https://doi.org/10.1007/s00445-013-0710-9

De Siena, L., Sammarco, C., Cornwell, D. G., La Rocca, M., Bianco, F., Zaccarelli, L., & Nakahara, H. (2018). Ambient seismic noise image of the structurally controlled heat and fluid feeder pathway at Campi Flegrei caldera. *Geophysical Research Letters*, *45*(13), 6428–6436. https://doi.org/10.1029/2018GL078817

Di Luccio, F., Persaud, P., Cucci, L., Esposito, A., Carniel, R., Cortés, G., et al. (2021). The seismicity of Lipari, Aeolian islands (Italy) from one-month recording of the LIPARI array. *Frontiers of Earth Science*, *9*, 678581. https://doi.org/10.3389/feart.2021.678581

Di Luccio, F., Persaud, P., Cucci, L., Esposito, A., Ventura, G., & Clayton, R. W. (2019). Seismic sensors probe Lipari's underground plumbing. *Eos*, *100*. https://doi.org/10.1029/2019EO125333

Dix, C. H. (1955). Seismic velocities from surface measurements. *Geophysics*, *20*(1), 68–86. https://doi.org/10.1190/1.1438126

Fang, H., Yao, H., Zhang, H., Huang, Y. C., & van der Hilst, R. D. (2015). Direct inversion of surface wave dispersion for three-dimensional shallow crustal structure based on ray tracing: Methodology and application. *Geophysical Journal International*, *201*(3), 1251–1263. https://doi.org/10.1093/gji/ggv080

Forni, F., Ellis, B. S., Bachmann, O., Lucchi, F., Tranne, C. A., Agostini, S., & Dallai, L. (2015). Erupted cumulated fragments in rhyolites from Lipari (Aeolian islands). *Contributions to Mineralogy and Petrology*, *170*(5–6), 49. https://doi.org/10.1007/s00410-015-1201-0

Forni, F., Lucchi, F., Peccerillo, A., Tranne, C. A., Rossi, P. L., & Frezzotti, M. L. (2013). Chapter 10: Stratigraphy and geological evolution of the Lipari volcanic complex (central Aeolian Archipelago). In F. Lucchi, A. Peccerillo, J. Keller, C. A. Tranne, & P. L. Rossi (Eds.), *The Aeolian islands volcanoes* (Vol. 37, pp. 213–279). Geological Society, London, Memoirs. https://doi.org/10.1144/M37.2

Govers, R., & Wortel, M. J. R. (2005). Lithosphere tearing at STEP faults: Response to edges of subduction zones. *Earth and Planetary Science Letters*, *236*(1), 505–523. https://doi.org/10.1016/j.epsl.2005.03.022

Granados, I., Calò, M., & Ramos, V. (2019). Noisy dispersion curve picking (NDCP): A Matlab package for group velocity dispersion picking of seismic surface waves. *Computers & Geosciences*, *133*, 104315. https://doi.org/10.1016/j.cageo.2019.104315

Granados-Chavarría, I., Calò, M., Figueroa-Soto, Á., & Jousset, P. (2022). Seismic imaging of the magmatic plumbing system and geothermal reservoir of the Los Humeros caldera (Mexico) using anisotropic shear wave models. *Journal of Volcanology and Geothermal Research*, *421*, 107441. https://doi.org/10.1016/j.jvolgeores.2021.107441

Haned, A., Stutzmann, E., Schimmel, M., Kiselev, S., Davaille, A., & Yelles-Chaouche, A. (2016). Global tomography using seismic hum. *Geophysical Journal International*, *204*(2), 1222–1236. https://doi.org/10.1093/gji/ggv516

Haney, M. M., & Tsai, V. C. (2017). Perturbational and non perturbational inversion of Rayleigh-wave velocities. *Geophysics*, *82*(3), F15–F28. https://doi.org/10.1190/geo2016-0397.1

Hansen, P. C. (1992). Analysis of discrete ill-posed problems by means of the L-curve. *SIAM Review*, *34*(4), 561–580. https://doi.org/10.1137/1034115

Jeddi, Z., Gudmundsson, O., & Tryggvason, A. (2017). Ambient-noise tomography of Katla volcano, south Iceland. *Journal of Volcanology and Geothermal Research*, *347*, 264–277. https://doi.org/10.1016/j.jvolgeores.2017.09.019

Lesage, P., Heap, M. J., & Kushnir, A. R. L. (2018). A generic model for the shallow velocity structure of volcanoes. *Journal of Volcanology and Geothermal Research*, *356*, 114–126. https://doi.org/10.1016/j.jvolgeores.2018.03.003

Liu, G., Persaud, P., & Clayton, R. W. (2018). Structure of the Northern Los Angeles Basins revealed in teleseismic receiver functions from short-term nodal seismic arrays. *Seismological Research Letters*, *89*(5), 1680–1689. https://doi.org/10.1785/0220180071

Matos, C., Silveira, G., Matias, L., Caldeira, R., Ribeiro, M. L., Dias, N. A., et al. (2015). Upper crustal structure of Madeira Island revealed from ambient noise tomography. *Journal of Volcanology and Geothermal Research*, *298*, 136–145. https://doi.org/10.1016/j.jvolgeores.2015.03.017

Mazzuoli, R., Tortorici, L., & Ventura, G. (1995). Oblique rifting in Salina, Lipari and Vulcano islands (Aeolian Islands, Southern Italy). *Terra Nova*, *7*(4), 444–452. https://doi.org/10.1111/j.1365-3121.1995.tb00540.x

Mordret, A., Roux, P., Boué, P., & Ben-Zion, Y. (2019). Shallow three-dimensional structure of the San Jacinto fault zone revealed from ambient noise imaging with a dense seismic array. *Geophysical Journal International*, *216*(2), 896–905. https://doi.org/10.1093/gji/ggy464

Neri, G., Caccamo, D., Cocina, O., & Montalto, A. (1996). Geodynamic implications of earthquake data in the southern Tyrrhenian sea. *Tectonophysics*, *258*(1–4), 233–249. https://doi.org/10.1016/0040-1951(95)00202-2

Nicolosi, I., Caracciolo, F., Branca, S., Ventura, G., & Chiappini, M. (2014). Volcanic conduit migration over a basement landslide at Mount Etna (Italy). *Scientific Reports*, *4*(1), 5293. https://doi.org/10.1038/srep05293

Ruch, J., Vezzoli, L., De Rosa, R., Di Lorenzo, R., & Acocella, V. (2016). Magmatic control along a strike-slip volcanic arc: The central Aeolian arc (Italy). *Tectonics*, *35*(2), 407–424. https://doi.org/10.1002/2015TC0040602016

Sabra, K. G., Gerstoft, P., Roux, P., Kuperman, W. A., & Fehler, M. C. (2005). Surface wave tomography from microseisms in Southern California. *Geophysical Research Letters*, *32*(14), L14311. https://doi.org/10.1029/2005GL023155

Saroglou, C., & Kallimogiannis, V. (2017). Fracturing process and effect of fracturing degree on wave velocity of a crystalline rock. *Journal of Rock Mechanics and Geotechnical Engineering*, *9*(5), 797–806. https://doi.org/10.1016/j.jrmge.2017.03.012

Schimmel, M., Stutzmann, E., & Gallart, J. (2011). Using instantaneous phase coherence for signal extraction from ambient noise data at a local to a global scale. *Geophysical Journal International*, *184*(1), 494–506. https://doi.org/10.1111/j.1365-246X.2010.04861.x

Shapiro, N. M., Campillo, M., Stehly, L., & Ritzwoller, M. H. (2005). High-resolution surface-wave tomography from ambient seismic noise. *Science*, *307*(5715), 1615–1618. https://doi.org/10.1126/science.1108339

Sieminsky, A., Lévêque, J.-J., & Debayleet, E. (2004). Can finite-frequency effects be accounted for in ray theory surface wave tomography? *Geophysical Research Letters*, *31*(24), L24614. https://doi.org/10.1029/2004GL021402

Sowers, T., & Boyd, O. S. (2019). Petrologic and mineral physics database for use with the U.S. Geological Survey National Crustal Model: U.S. Geological Survey Open-File Report 2019–1035, 17 p., https://doi.org/10.3033/ofr20191035

Spica, Z., Perton, M., Calò, M., Legrand, D., Córdoba-Montiel, F., & Iglesias, A. (2016). 3-D shear wave velocity model of Mexico and south US: Bridging seismic networks with ambient noise cross-correlations (c1) and correlation of coda of correlations (c3). *Geophysical Journal International*, *206*(3), 1795–1813. https://doi.org/10.1093/gji/ggw240

Spica, Z., Perton, M., & Legrand, D. (2017). Anatomy of the Colima volcano magmatic system, Mexico. *Earth and Planetary Science Letters*, *459*, 1–13. https://doi.org/10.1016/j.epsl.2016.11.010

Stankiewicz, J., Ryberg, T., Haberland, C., & Natawidjaja, D. (2010). Lake Toba volcano magma chamber imaged by ambient seismic noise tomography. *Geophysical Research Letters*, *37*(17), L17306. https://doi.org/10.1029/2010GL044211

Townsend, M. R., Pollard, D. D., & Smith, R. P. (2017). Mechanical models for dikes: A third school of thought. *Tectonophysics*, *703–704*, 98–118. https://doi.org/10.1016/j.tecto.2017.03.008

Ventosa, S., Schimmel, M., & Stutzmann, E. (2017). Extracting surface waves, hum and normal modes: Time-scale phase-weighted stack and beyond. *Geophysical Journal International211*(1), 30–44. https://doi.org/10.1093/gji/ggx284

Ventura, G., Vilardo, G., Milano, G., & Pino, N. A. (1999). Relationships among crustal structure, volcanism and strike-slip tectonics in the Lipari-Vulcano volcanic complex (Aeolian Islands, Southern Tyrrhenian Sea, Italy). *Physics of the Earth and Planetary Interiors*, *116*(1–4), 31–52. https://doi.org/10.1016/s0031-9201(99)00117-x

Wang, Y., Lin, F.-C., Schmandt, B., & Farrell, J. (2017). Ambient noise tomography across Mount St. Helens using a dense seismic array. *Journal of Geophysical Research: Solid Earth*, *122*(6), 4492–4508. https://doi.org/10.1002/2016JB013769

Yang, Y., Ritzwoller, M. H., Lin, F.-C., Moschetti, M. P., & Shapiro, N. M. (2008). Structure of the crust and uppermost mantle beneath the western United States revealed by ambient noise and earthquake tomography. *Journal of Geophysical Research*, *113*(B12), B12310. https://doi.org/10.1029/2008JB005833